Hyperfine characterization and spin coherence lifetime extension in Pr^{3+}:$La_2(WO_4)_3$

Marko Lovrić,* Philipp Glasenapp, and Dieter Suter
Technische Universität Dortmund, Fachbereich Physik, D-44221 Dortmund, Germany

Biagio Tumino, Alban Ferrier, and Philippe Goldner†
Chimie ParisTech ENSCP, Laboratoire de Chimie de la Matiére Condensée de Paris (LCMCP), F-75005 Paris, France UPMC Univ Paris 06, F-75005 Paris, France CNRS, UMR 7574, F-75005 Paris, France

Mahmood Sabooni, Lars Rippe, and Stefan Kröll
Department of Physics, Lund University, P.O. Box 118, S-221 00 Lund, Sweden

(Received 27 June 2011; revised manuscript received 11 August 2011; published 12 September 2011)

Rare-earth ions in dielectric crystals are interesting candidates for storing quantum states of photons. A limiting factor on the optical density and thus the conversion efficiency is the distortion introduced in the crystal by doping elements of one type into a crystal matrix of another type. Here we investigate the system Pr^{3+}:$La_2(WO_4)_3$, where the similarity of the ionic radii of Pr and La minimizes distortions due to doping. We characterize the praseodymium hyperfine interaction of the ground-state ($^3H_4$) and one excited state ($^1D_2$) and determine the spin Hamiltonian parameters by numerical analysis of Raman-heterodyne spectra, which were collected for a range of static external magnetic-field strengths and orientations. On the basis of a crystal-field analysis, we discuss the physical origin of the experimentally determined quadrupole and Zeeman tensor characteristics. We show the potential for quantum memory applications by measuring the spin coherence lifetime in a magnetic field that is chosen such that additional magnetic fields do not shift the transition frequency in first order. Experimental results demonstrate a spin coherence lifetime of 158 ms — almost 3 orders of magnitude longer than in zero field.

DOI: 10.1103/PhysRevB.84.104417 PACS number(s): 42.50.Md, 76.30.Kg, 76.70.Hb, 76.60.−k

I. INTRODUCTION

Rare-earth ion-doped crystals (REICs) have recently appeared as promising solid-state materials for quantum information processing. In the field of quantum computing, achieved milestones include controlled phase gates[1] and single-qubit arbitrary rotation.[2] While these experimental results were performed on single-qubit and two-qubit systems, scalable schemes have also been proposed.[3] In the field of quantum memories, devices able to faithfully store and release photonic quantum states have been proposed and implemented. Using several different storage-recall protocols,[4–7] high-efficiency,[8] multiple-photon storage with large bandwidth[9,10] and entanglement storage[11,12] were demonstrated in REICs. These results rely on the very long optical coherence lifetimes, e.g., 4.4 ms lifetimes have been observed in Er^{3+}:Y_2SiO_5.[13]

Even longer lifetimes have been reported for rare-earth ion hyperfine transitions and accordingly, the qubit in REIC-based quantum computing and memories is generally defined by selecting two ground-state hyperfine levels. Optical transitions are used to selectively address qubits or to transfer coherences from the optical to the rf domain and vice versa. Coherence lifetimes can be extended to 30 s for a ground-state hyperfine transition of Pr^{3+}:Y_2SiO_5 at liquid helium temperature.[14] This was achieved in two steps: First, an external magnetic field was applied to the sample in order to decouple one hyperfine transition from magnetic-field fluctuations due to host spin flips. As these are the main source of dephasing, the zero-field coherence lifetime of 500 μs was extended in this way to 82 ms[15] and later to 860 ms.[14] The decoupling was achieved by minimizing the transition energy dependence with respect to the magnetic field. This condition is referred as ZEFOZ, or zero-first-order Zeeman shift transitions.[16] The coherence lifetime was then further increased by rf decoupling pulses arranged in a Carr-Purcell sequence.[14]

Y_2SiO_5 is the most thoroughly studied host in REIC quantum information processing. It combines long coherence lifetimes, favored by its low-magnetic-moment density, mainly due to Y nuclear spins, and high oscillator strengths. A disadvantage of Y-based host material is that doping with Pr^{3+} or Eu^{3+} leads to relatively large inhomogeneous linewidths at high doping concentrations, which limits the maximal achievable optical depth. This is an important concern in high-efficiency quantum memories.[17] To overcome this limitation for Pr^{3+}, we proposed a La-based crystal, $La_2(WO_4)_3$. Pr^{3+} substitutes La^{3+} in this material, both having very similar ionic radii ($r_{La^{3+}} = 1.18$ Å, $r_{Pr^{3+}} = 1.14$ Å).[18] Compared to Y_2SiO_5 ($r_{Y^{3+}} = 1.02$ Å),[18] doping stress is reduced and the inhomogeneous linewidth is 15 times smaller for high Pr^{3+}concentrations. However, the magnetic moment of lanthanum (2.78 μ_B) is much higher than that of Y^{3+} (-0.14 μ_B), and the $La_2(WO_4)_3$ magnetic-moment density is 7.5 times higher than in Y_2SiO_5. It seems that this should be seriously detrimental to coherence lifetimes, but we measured a hyperfine lifetime of 250 μs,[19] which is only smaller by a factor of $\approx$2 compared to the value in Y_2SiO_5. This allowed us to measure narrow and efficient electromagnetically induced transparency in this material.[20] This result also suggested that REICs that could be useful for quantum information processing are not limited to the few crystals with very low-magnetic-moment density. However, since applications require T_2 values in the millisecond range, techniques for increasing the coherence lifetime should be used. In this paper we show that by using a ZEFOZ transition hyperfine T_2 can

reach 158 ± 7 ms, corresponding to a 630-fold increase. It is therefore possible to strongly reduce the influence of host spin flips, even in the case of high-magnetic-moment density.

ZEFOZ transitions appear at specific magnetic field vectors, which can only be predicted if all parameters of the system Hamiltonian are known with high precision. In the present system, the $I = 5/2$ nuclear spin of ^{141}Pr (100% abundance) and the C_1 site symmetry result in a complicated hyperfine structure. We therefore used the approach of Ref. 21, which consists of determining the spin Hamiltonian parameters by coherent Raman scattering before numerically identifying ZEFOZ transitions. Finally, the coherence lifetimes of the hyperfine transitions were measured by optically detected Raman echoes.

II. MODEL FOR THE HYPERFINE INTERACTION

A good approximation for the Hamiltonian of many rare-earth-doped compounds is[22]

$$\mathcal{H}_0 = [\mathcal{H}_{\mathrm{FI}} + \mathcal{H}_{\mathrm{CF}}] + [\mathcal{H}_{\mathrm{HF}} + \mathcal{H}_Q + \mathcal{H}_Z + \mathcal{H}_z]. \tag{1}$$

The first two terms, the free ion (including spin-orbit coupling), and the crystal-field Hamiltonians determine the energies of the electronic degrees of freedom. The terms in the second bracket, consisting of the hyperfine coupling, the nuclear quadrupole coupling, and the electronic and the nuclear Zeeman Hamiltonian, lift the degeneracy of the nuclear-spin states.

The site symmetry of our system is low enough that the electronic states are nondegenerate. As a result of this "quenching" of the electronic angular momentum, the electronic Zeeman $\mathcal{H}_Z$ and hyperfine interaction $\mathcal{H}_{\mathrm{HF}}$ contribute only as second-order perturbations. Utilizing this, the four last terms of Eq. (1) can be well approximated by a nuclear-spin Hamiltonian[22,23]:

$$\mathcal{H}_1 = \vec{B} \cdot \mathbf{M}_1 \cdot \vec{I} + \vec{I} \cdot \mathbf{Q}_1 \cdot \vec{I}, \tag{2}$$

$$\mathbf{M}_1 = R_M \cdot \begin{bmatrix} g_x & 0 & 0 \\ 0 & g_y & 0 \\ 0 & 0 & g_z \end{bmatrix} \cdot R_M^T, \tag{3}$$

$$\mathbf{Q}_1 = R_Q \cdot \begin{bmatrix} E - \frac{1}{3}D & 0 & 0 \\ 0 & -E - \frac{1}{3}D & 0 \\ 0 & 0 & \frac{2}{3}D \end{bmatrix} \cdot R_Q^T, \tag{4}$$

where the $R_i = R(\alpha_i, \beta_i, \gamma_i)$ represent rotation matrices and Euler angles[24] (see Sec. II in Ref. 25), specifying the orientation of the effective Zeeman tensor $\mathbf{M}$ and the effective quadrupolar tensor $\mathbf{Q}$ principal axis system (PAS) [(x', y', z') and (x'', y'', z''), respectively] relative to the laboratory-based reference axis system (x, y, z) (see Sec. III). In general, the $\mathbf{M}$ and $\mathbf{Q}$ principal axes are not aligned and accordingly, the R_Q and R_M matrices are not identical.

In zero magnetic field, the quadrupole interaction results in a partial lifting of the nuclear-spin states degeneracy. The corresponding structures for lowest levels of the crystal-field multiplets $^3H_4$ and $^1D_2$ were determined by hole-burning experiments[19,26] and are shown in Fig. 1. We label the levels

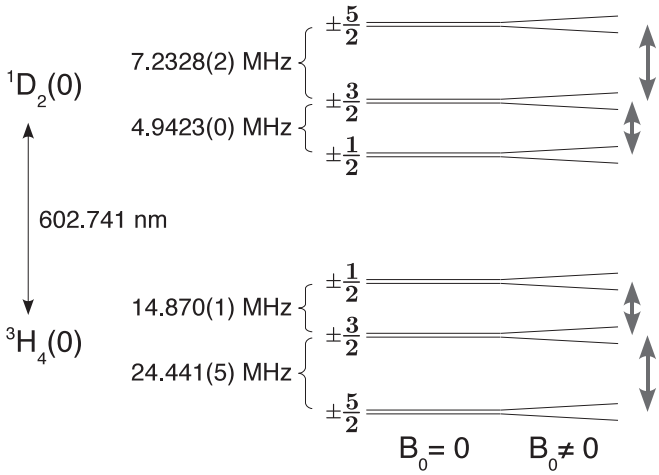

FIG. 1. Pr^{3+}:$La_2(WO_4)_3$ level structure of the lowest (0) $^3H_4$ and $^1D_2$ crystal-field manifolds, including their hyperfine structure. The order of the energy levels follows from previous work,[19] whereas the transition frequencies given above could be measured with higher precision utilizing zero-field Raman-heterodyne scattering within the present work. The arrows on the right indicate the range of hyperfine transitions excited by rf in the separate experiments.

by their projections onto the z'' principal axes of the $\mathbf{Q}$ tensor, noting that these states are not eigenstates of the nuclear-spin Hamiltonian. Since the PAS of the $\mathbf{Q}$ tensors of different crystal-field levels do not coincide, their quantization axes are also different. For the small magnetic fields used to determine spin Hamiltonian parameters, the hyperfine structure remains close to the zero-field one, which allows us to identify resonance lines with transitions between zero-field states.

Since Pr^{3+} occupies two different subsites in the crystal (see Sec. III), the Hamiltonian describing the second site includes different rotation matrices. Utilizing Eq. (2) of site 1 and the property that both sites are connected by a C_2 symmetry we write

$$\mathcal{H}_2 = \vec{B} \cdot \left(R_{C_2} \mathbf{M}_1 R_{C_2}^T\right) \cdot \vec{I} + \vec{I} \cdot \left(R_{C_2} \mathbf{Q}_1 R_{C_2}^T\right) \cdot \vec{I}. \tag{5}$$

With

$$R_{C_2} = R_C^T \cdot R_\pi \cdot R_C,$$
$$R_C = R(\alpha_{C_2}, \beta_{C_2}, 0), \quad R_\pi = R(180^\circ, 0, 0),$$

the angles α_{C_2} and β_{C_2} correspond to the spherical coordinates of the C_2 axis in the laboratory system. Therefore in this manuscript the complete nuclear-spin Hamiltonian of a given crystal-field level depends on 13 parameters: $D, E, \alpha_Q, \beta_Q, \gamma_Q, g_x, g_y, g_z, \alpha_M, \beta_M, \gamma_M, \alpha_{C_2}, \beta_{C_2}$.

III. EXPERIMENT

We used a sample of high optical quality, grown by the Czochralski method, containing 0.2 at. % Pr^{3+}. The $5 \times 5 \times 5$ mm crystal was mounted in an optical cryostat and cooled to liquid helium temperatures. $La_2(WO_4)_3$ forms a monoclinic crystal with a $C2/c$ space group, identical to that of Y_2SiO_5. The La^{3+} ions occupy only one crystallographic site of C_1 symmetry. In each unit cell (containing four formula units), this site appears at eight positions which are related by inversion,

translation, and C_2 symmetries. The C_2 axes are identical to the C_2 crystal symmetry axis, also denoted by b in the following. The C_2 symmetry divides the La positions into two groups of four ions, which behave differently, unless the magnetic field is perpendicular or parallel to the b axis. These two groups are called subsites in the following. The crystal surfaces were polished perpendicular to the (X,Y,Z) principal axes of the optical indicatrix. Optical back reflection at the Z surface and mechanical alignment of the X and Y surfaces was used to align the crystal along our reference (x,y,z) axes, defined by the static magnetic-field coils (see below). Apart from alignment errors the (X,Y,Z) axes should be a replica of (x,y,z), the laser propagating along the z/Z and the b/Y axis expected to be closely aligned to the laboratory-frame y axis.

To obtain the hyperfine spectra of both the electronic ground-state and the electronically excited state, we used Raman-heterodyne scattering (RHS).[27,28] In this scheme a resonant rf field creates coherence between two hyperfine levels. Prior to this, the laser can be used to create initial population between those states. The laser further serves to transfer the hyperfine coherence into the optical transition and can simultaneously be used as the local oscillator for a heterodyne detection of the excited Raman field, as the latter is coherently emitted into the same optical mode.

A Coherent 899-21 dye laser, further stabilized by home-built electronics with respect to intensity and frequency (linewidth <20 kHz), served as the light source. It was tuned to the center of the $^3H_4(0) \leftrightarrow {}^1D_2(0)$ transition (see Fig. 1). The laser was focused, from a collimated beam of 1.5 mm diameter, with a 300-mm lens into the sample. We generated the optical pulses and frequency chirps by double-pass acousto-optic modulator setups.

The rf fields were applied to the sample by a ten-turn 6-mm-diameter coil. For continuous-wave experiments (ground-state), one side of the coil was terminated by a 50-Ω load, and the other was attached to an rf driver. For the exited state spectra, we used a pulsed RHS scheme. Here the coil was part of an appropriate tuned tank circuit. Figure 2 shows the sequences used for the two types of experiments.

The frequencies for the rf excitation and the shifting of the laser frequency were generated by 48-bit, 300-MHz direct digital synthesizers, yielding very precise frequencies. We controlled the timing of the pulses and frequency chirps by a word generator with a resolution of 4 ns. Detection of the heterodyne beat signal was accomplished by a 100-MHz balanced photo receiver (Femto HCA-S), a phase-sensitive quadrature-detection demodulation scheme, appropriate analog and digital filters, and a digital oscilloscope.

The static magnetic field was created by a set of three orthogonal Helmholtz coil pairs. They are mounted outside the cryostat and their coil diameters range from 20 to 40 cm, providing a homogeneous field over the sample volume in their center. With currents of about 10 A, each coil pair generates a magnetic field of about 8 mT. To control the field vector a computer control was set up for the current sources of the Helmholtz coils. To compensate nonlinearities and drifts, we used a set of three orthogonal Hall probes as sensors for a computer-based feedback loop. The absolute error of the field components is <0.06 mT, and the relative linear error for the static magnetic field is <0.3%. To minimize the effect of

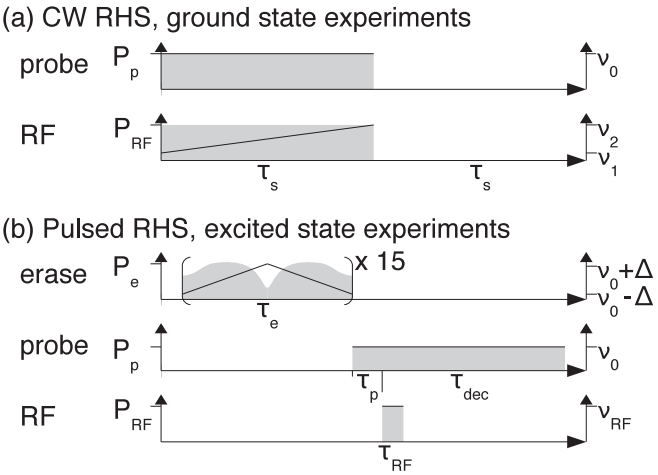

FIG. 2. RHS pulse sequences. Black lines indicate frequencies and gray areas the applied optical and rf powers. (a) Continuous-wave sequence for the ground-state measurements. A low-power laser probe ($P_p = 0.3$ mW) and a scanning frequency rf ($P_{\mathrm{RF}} \approx 1$ W, $\tau_s = 50$ ms, $\nu_1 = 7.4$, and $\nu_2 = 22.4$ MHz for $|\pm\frac{1}{2}\rangle \leftrightarrow |\pm\frac{3}{2}\rangle$ or, respectively, 17.1 and 32.1 MHz for $|\pm\frac{3}{2}\rangle \leftrightarrow |\pm\frac{5}{2}\rangle$) were applied to the sample. The optimum temperature of the cold finger for this scheme was 4.5 K, since still lower temperatures gave such slow hyperfine level relaxation rates that it would be necessary to repump the hyperfine level population. (b) Pulsed RHS sequence for the excited state. Probe and erase beam were overlapped in the sample at an angle of 0.6°. To allow for higher repetition rate the chirped erase laser ($\Delta = 64$ MHz, $\tau_e = 10$ ms, average power $P_e \approx 20$ mW) redistributed the populations. An initial population difference between hyperfine sublevels was created by the probe beam ($P_p = 1.2$ mW, $\tau_p = 100$ μs) and converted to coherences by an rf pulse ($\nu_{\mathrm{RF}} = 4.94/7.23$ MHz ($|\pm\frac{1}{2}\rangle \leftrightarrow |\pm\frac{3}{2}\rangle$ resp. $|\pm\frac{3}{2}\rangle \leftrightarrow |\pm\frac{5}{2}\rangle$), $P_{\mathrm{RF}} = 214/287$ W, $\tau_{\mathrm{RF}} = 4$ μs). For optical heterodyne detection the same probe beam was left active for an additional time τ_{dec}. The temperature of the cold finger for this scheme was 2.4 K.

small background fields (e.g., earth magnetic field), a small compensation field was used, which minimized the observed zero-field RHS line splitting and also led to almost perfect destructive interference.[29,30] We used this compensation field as our zero-field reference in all measurements.

For an optimal determination of the Hamiltonian parameters, it is important to sample different strengths and orientations of the magnetic field. In our experiments we used a spiral on the surface of an ellipsoid[21]:

$$\vec{B}(t) = \begin{pmatrix} B_x\sqrt{1-t^2}\cos(6\pi t) \\ B_y\sqrt{1-t^2}\sin(6\pi t) \\ B_z t \end{pmatrix}. \tag{6}$$

Here, we use

$$t = -1 + (N-1)\frac{2}{N_{\mathrm{tot}}-1}, \quad N = 1,2,\ldots,N_{\mathrm{tot}}$$

to represent the discrete coordinate along the trajectory. For the ground-state series, we measured $N_{\mathrm{tot}} = 101$ orientations, with magnetic-field amplitudes $[B_x,B_y,B_z] = [7,8,9]$ mT and for the excited state we used $N_{\mathrm{tot}} = 251$ and

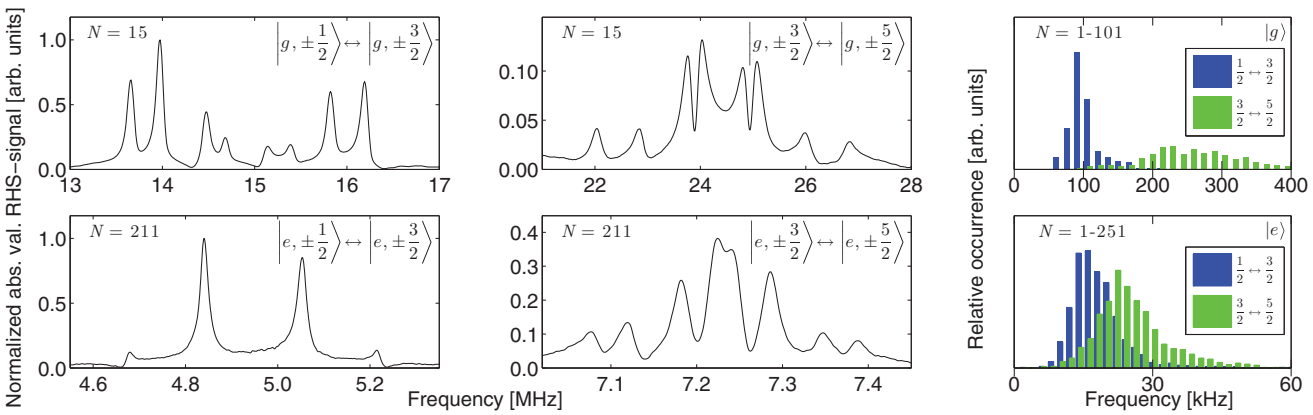

FIG. 3. (Color online) Representative ground- (cw) and exited-state (pulsed) RHS spectra. Both spectra from the ground-state ($|g,i \leftrightarrow j\rangle$) are recorded at $\vec{B} = (2.60,-5.27,-5.76)$ mT. For the excited state spectra, we used $\vec{B} = (4.62,1.19,4.42)$ mT. The normalization is relative to the largest line from ground- or excited state spectra, respectively. The $|g,i \leftrightarrow j\rangle$ spectra shown here resolve all $8+8$ possible RHS transitions, while in the $|e,i \leftrightarrow j\rangle$ spectra not all lines are resolved. The histograms on the right show the distributions of fitted FWHM RHS linewidths for all recorded data (see Sec. IA in Ref. 25), plotted separately for the two hyperfine transitions ($|g/e,i \leftrightarrow j\rangle$, $i/j = \pm\frac{1}{2}/\pm\frac{3}{2}$ or $\pm\frac{3}{2}/\pm\frac{5}{2}$). For both the ground- and the excited state, the $\pm\frac{3}{2} \leftrightarrow \pm\frac{5}{2}$ linewidths are bigger (see Sec. V C). The mean linewidths are $|g,\pm\frac{1}{2} \leftrightarrow \pm\frac{3}{2}\rangle \approx 105$ kHz, $|g,\pm\frac{3}{2} \leftrightarrow \pm\frac{5}{2}\rangle \approx 301$ kHz, $|g,\text{all}\rangle \approx 196$ kHz and $|e,\pm\frac{1}{2} \leftrightarrow \pm\frac{3}{2}\rangle \approx 18.3$ kHz, $|e,\pm\frac{3}{2} \leftrightarrow \pm\frac{5}{2}\rangle \approx 26.3$ kHz, $|e,\text{all}\rangle \approx 22.3$ kHz.

$B_x = B_y = B_z = 6.5$ mT. Figure 3 shows some typical experimental spectra for the ground- and excited states.

IV. THE FITTING PROCEDURE

As described in Sec. II, 13 parameters are necessary to fully characterize the spin Hamiltonian in the laboratory. Using those it is possible to compute the line positions in the RHS spectra. By minimization of the the rms deviation [see Eq. (14) in Ref. 25] between calculated and experimental line positions, the spin Hamiltonian parameters can be derived. Due to the large number of parameters and their complicated interdependency, gradient-based algorithms are not efficient, as they tend to stick to local minima. In our case the combination of first running a probabilistic and then a direct search yielded the best convergence to the global minimum. As in the work of Longdell *et al.*,[16,21] we used simulated annealing[31] for the first step. It allows for robust convergence to a global minimum when using appropriate settings. The latter typically cause simulated annealing to converge relatively slowly, although being already close to the global minimum in advanced phases. Therefore we switch to a pattern search[32] algorithm in this situation. We provide additional details of the fitting procedure in the supplementary material.[25]

The underlying symmetry of the crystal-field and the structure of the spin Hamiltonian cause some ambiguity if only RHS spectra are used to determine the Hamiltonian parameters.[33] Important for our investigation is the fact that the RHS spectra do not depend on the signs of D, E, and the gyromagnetic factors g_x, g_y, and g_z. In addition, different sets of Euler angles correspond to the same tensor orientations. As a consequence, different runs with random initial values lead to apparently different solutions. We checked that these solutions are related by the symmetry operations mentioned above and thus verified that we really found a unique global minimum.

V. RESULTS

A. Electronic ground-state

Figure 4(a) shows the experimental data for $N_{\text{tot}} = 101$ different external magnetic fields. Several fit trails reliably led to the parameters shown in Table I and represented by the solid lines in Fig. 4(a). All quoted Euler angles are given in the "zyz" convention.[24]

With these parameters, the rms deviation between all accounted line positions and the fit is ≈32 kHz, significantly smaller than the average linewidth of the ground-state RHS lines of ≈196 kHz (see Fig. 3), indicating that it is dominated by statistical error. At the end of the fitting procedure, $L = 1218$ of the total 1221 experimental lines could be unambiguously assigned (see Sec. I B in Ref. 25) to calculated resonance line positions.

To estimate the uncertainty of the fitted parameters, we sampled the parameter space in the vicinity of the global minimum by repeating the probabilistic part of the fitting procedure using a fixed, low-temperature T_σ. Such a procedure can be shown to be rigorous if the only source of error is Gaussian noise in the line positions.[21,33] To estimate this noise we used the mean ratio of fitted linewidths σ_i to the individual signal-to-noise ratio (SNR_i) for all contributing RHS lines:

$$\nu_\sigma = \frac{1}{L}\sum_{i=1}^{L}\frac{\sigma_i}{SNR_i}.$$

For the ground-state data we found $\nu_\sigma = 1.4$ kHz. According to this we chose the fixed temperature T_σ, so that a single parameter change from its optimum value by T_{σ_i}(see Sec. I B in Ref. 25) resulted in an increase of the rms deviation by ν_σ. After 2×10^6 iterations the histograms of the accepted parameters all showed a Gaussian shape, whose 1σ widths are given as fit error in Table I.

Apart from the statistical error, we also consider systematic errors. The most important contribution is due to the calibration

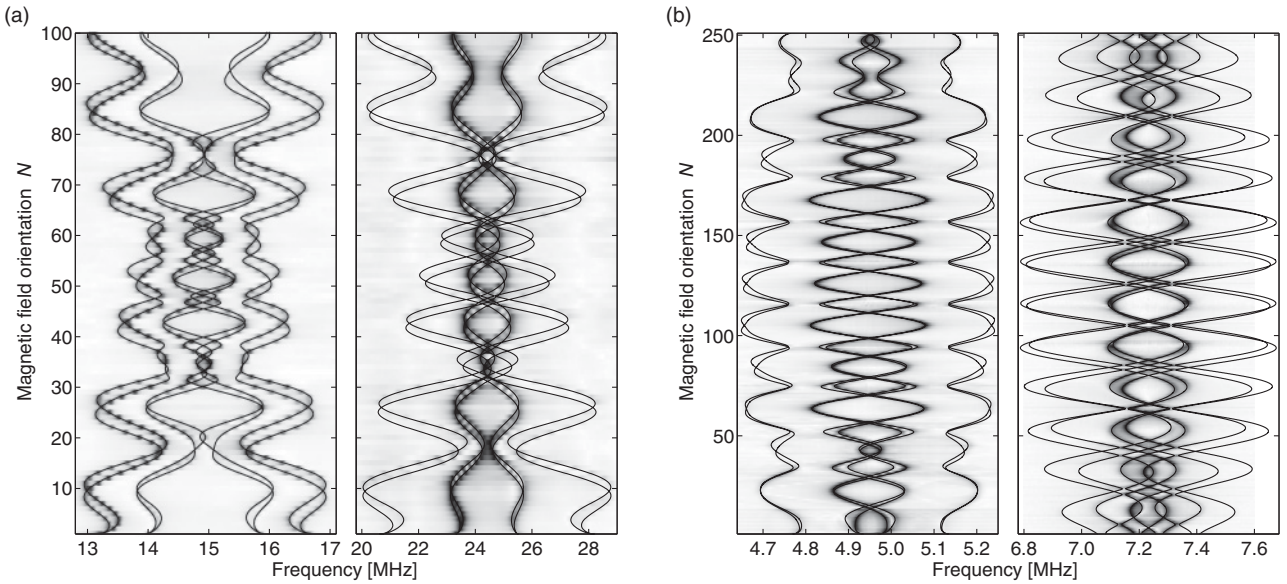

FIG. 4. RHS spectra of the $|\pm\frac{1}{2}\rangle \leftrightarrow |\pm\frac{3}{2}\rangle$ and $|\pm\frac{3}{2}\rangle \leftrightarrow |\pm\frac{5}{2}\rangle$ hyperfine transitions. (a) $^3H_4(0)$ ground-state cw RHS spectra. (b) $^1D_2(0)$ excited state pulsed RHS spectra. In both cases the solid lines represent the fit results and the shaded background the absolute value of the experimental spectra. For each field orientation, the spectrum was normalized to the maximum signal amplitude.

error of the magnetic field. We estimate its precision to ≈0.65%, which translates to the same fractional uncertainty of the gyromagnetic ratios g_x, g_y, and g_z. As the parameters are given in the laboratory-fixed reference frame (x,y,z), a misalignment of the crystal does not contribute to the error but is expressed by the α_{C_2} and β_{C_2} values not being exactly 90°. The only systematic contribution in the angles arises from the nonorthogonality of the coils, which is $<1°$. The uncertainty of the alignment of the crystal relative to our reference (x,y,z) and that of the crystal surfaces to the optical indicatrix (X,Y,Z) results in an error of $\approx 5°$ for the angles seen relative to the crystal axis system.

B. Excited state

With the optimal fit parameters, we found an rms deviation of 3.1 kHz between theoretical and experimental frequency values, using $L = 2345$ of the 2353 measured lines in $N_{\text{tot}} = 251$ spectra. Compared to the mean experimental full width at half maximum (FWHM) of 22.3 kHz, the rms deviation is even better than for the ground-state. We mainly attribute this to the higher quality of pulsed RHS spectra, with fewer line-shape artifacts. Figure 4(b) and Table II show the results.

For the determination of the fit errors here we found $\nu_\sigma = 136$ Hz. The systematic errors are again dominated by the calibration error of the magnetic field. We note that although the crystal was remounted between this and the ground-state experiments, the resulting orientation of the C_2 axis deviates less than our estimated alignment accuracy. As the Zeeman tensor is almost axially symmetric, $g_x \approx g_z$, its orientation relative to the quadrupole tensor or to the ground-state tensor orientations cannot be determined accurately.

C. Discussion

Examining Tables I and II, it appears that the principal values for the **Q** and **M** tensors are similar to those found in other hosts like Y_2SiO_5,[21] LaF_3, or $YAlO_3$.[22] Especially, the

TABLE I. Ground-state spin Hamiltonian parameters.

Parameter	Value	Fit error	Unit
D	−6.3114	0.0027	MHz
E	−0.8915	0.0021	MHz
α_Q	20.4	3.3	deg.
β_Q	147.7	1.4	deg.
γ_Q	10.2	1.4	deg.
g_x	−51.7	3.6	MHz/T
g_y	−23.5	1.1	MHz/T
g_z	−146.97	0.75	MHz/T
α_M	30.1	3.8	deg.
β_M	146.59	0.55	deg.
γ_M	13.09	0.69	deg.
α_{C_2}	88.34	0.47	deg.
β_{C_2}	92.45	0.31	deg.

TABLE II. Excited state spin Hamiltonian parameters.

Parameter	Value	Fit error	Unit
D	1.90705	0.00023	MHz
E	0.35665	0.00014	MHz
α_Q	−18.51	0.71	deg.
β_Q	73.83	0.48	deg.
γ_Q	−84.22	0.37	deg.
g_x	−17.22	0.27	MHz/T
g_y	−14.39	0.10	MHz/T
g_z	−18.37	0.14	MHz/T
α_M	−23.7	2.4	deg.
β_M	88.5	4.1	deg.
γ_M	−80.1	1.8	deg.
α_{C_2}	88.63	0.25	deg.
β_{C_2}	92.69	0.24	deg.

ground-state gyromagnetic tensor is anisotropic with one large component, in contrast to the excited state which also exhibits smaller values. To get some insight into these properties, we compared these results with calculations derived from crystal-field calculations.

In a previous work[34] we found that quadrupolar D and E values for ground- and excited states could be very well reproduced starting from electronic wave functions obtained by a crystal-field analysis. The latter was done assuming a C_{2v} site symmetry, which is higher than the actual one (C_1). In this higher symmetry, the **Q** tensors for different crystal-field levels are colinear, in clear contradiction with our results. Nevertheless, it seems that the additional crystal-field parameters of C_1 symmetry have little effect on the **Q** principal values. In the following we present the calculations of the **M** tensor principal values.

In C_{2v} orthorhombic symmetry, the spin Hamiltonian of Eq. (2), expressed in the (x_c, y_c, z_c) crystal-field axes, reads

$$\mathcal{H}'' = \sum_{i=x_c,y_c,z_c} B_i g_i I_i + D\left(I_{z_c}^2 - \frac{I(I+1)}{3}\right) + E\left(I_{x_c}^2 - I_{y_c}^2\right), \quad (7)$$

where the g_i are related to a tensor $\mathbf{\Lambda}$[23]:

$$g_i = -2A_J g_J \mu_B \Lambda_{ii} - g_I \mu_N. \quad (8)$$

The Λ tensor is given by

$$\Lambda_{\alpha\beta} = \sum_{n=1}^{2J+1} \frac{\langle 0|J_\alpha|n\rangle\langle n|J_\beta|0\rangle}{E_n - E_0} \quad (9)$$

and can be calculated from the electronic wave functions $|n\rangle$. The latter were found using a free ion and crystal-field Hamiltonian whose parameters were fitted to experimentally determined crystal-field levels E_n.[34] In this calculation, we use arbitrary permutations of the (x_c, y_c, z_c) axes. This results in different sets of E and D values, which give the same hyperfine energy levels. We subsequently fix the choice of the axis system such that the convention $0 \leqslant 3E/D = \eta \leqslant 1$[35] is fulfilled, thereby resolving ambiguous sets of parameters, such as (in megahertz) $D = -1.8184$, $E = 3.6014$ and $D = -6.3114$, $E = -0.8915$, which describe identical ground-state zero-field hyperfine structures and correspond to an exchange of x_c with z_c. With this convention, we fix the permutation of the axes and thus the values for D and E for both electronic states. The crystal-field parameters we used and the corresponding E and D values for the ground- and excited states are listed in Table III.[36] The electronic wave function of the excited $^1D_2(1)$ level is used instead of that of $^1D_2(0)$ to take into account a wrong ordering in the calculated crystal-field levels of this multiplet.[34,37]

Comparing Tables I and II with Table III shows that a reasonable agreement is found between experimental and calculated principal values of ground- and excited state **M** tensors. Again, this suggests that additional parameters appearing in calculations using C_1 symmetry mainly determine the relative orientation between the different tensors. Calculated values especially reproduce the two features mentioned above: the very large value of g_z for the ground-state and the smaller g_i values for the excited state compared to the ground-state. A qualitative understanding of these properties can be obtained from the crystal-field analysis by looking at the different factors entering in Eq. (8) (see Table III). We first note that the isotropic and crystal-field independent nuclear Zeeman contribution to g_i equals −12.2 MHz/T. Differences in g_i values are mainly linked to the $\mathbf{\Lambda}$ tensors, since the products $A_J g_J$ vary by only 4% between ground- and excited states. The $\mathbf{\Lambda}$ tensors involve the $\vec{J}$ matrix elements and the energy differences appearing as denominators in Eq. (9). We first discuss the ground-state case. The electronic wave function of interest [$^3H_4(0)$] has the following form:

$$|0\rangle = -0.62|^3H_4,-4\rangle - 0.62|^3H_4,4\rangle - 0.4|^3H_4,0\rangle,$$

where brackets on the right-hand side are written as $|^{2S+1}L_J, M_J\rangle$ and only terms with a coefficient larger than 0.15 have been kept. The larger J_{z_c} matrix element is found between $|0\rangle$ and $|1\rangle$, since the latter is nearly only composed of $|^3H_4,\pm4\rangle$ states. The $|\langle 0|J_{z_c}|1\rangle|$ matrix element equals 3.6 close to the maximum value of $|\langle ^3H_4,\pm4|J_{z_c}|^3H_4,\pm4\rangle| = 4$. Moreover, this large matrix element is found for levels close in energy (65 cm^{-1} Ref. 34), resulting in a large $\Lambda_{z_c z_c}$. On the other hand, $|0\rangle$ couples to crystal-field levels containing $|^3H_4,\pm3\rangle$, $|^3H_4,\pm1\rangle$ by J_{x_c} or J_{y_c} operators. The corresponding matrix elements do not exceed 2.4 in absolute value. As expected, this is close to the average value of matrix elements of the form $\langle ^3H_4,\pm4|J_i|^3H_4,\pm3\rangle$ and $\langle ^3H_4,\pm1|J_i|^3H_4,\pm2\rangle$ (where $i = x_c$ or y_c), which is at most 1.9. The levels with the largest matrix elements are located at high energies ($E_3 = 143$ and $E_5 = 349$ cm^{-1} for J_{y_c} and J_{x_c}, respectively), resulting in low $\Lambda_{x_c x_c}$ and $\Lambda_{y_c y_c}$. This in turn explains the small values of g_{x_c} and g_{y_c} compared to g_{z_c}.

A similar analysis can be performed for the excited state. As mentioned above, the level of interest is $^1D_2(1)$ and is found to be equal to

$$|1\rangle = 0.67|^1D_2,-2\rangle - 0.67|^1D_2,2\rangle,$$

with the same convention as above. This state gives a J_{z_c} matrix element equal to 2 with the state $|4\rangle$, located 441 cm^{-1} higher than $|1\rangle$. Maximum average values for matrix elements of J_{x_c} and J_{y_c} can be estimated as above for levels containing $|^1D_2 \pm 1\rangle$ states, resulting in $|\langle 0|J_{x_c}|1\rangle| \approx |\langle 1|J_{x_c}|2\rangle| \approx 1$. The corresponding energies are

TABLE III. Crystal-field parameters B_{ij}, calculated **Q** and **M** tensor principal values, and second-order hyperfine interaction parameters.

B_{ij}	(cm^{-1})		Ground-state	Excited state	Unit
B_{20}	375	D	−6.1	2.0	MHz
B_{22}	−93	E	−0.63	0.30	MHz
B_{40}	768	g_{x_c}	−32	−18	MHz/T
B_{42}	445	g_{y_c}	−22	−4	MHz/T
B_{44}	1027	g_{z_c}	−151	−18	MHz/T
B_{60}	267	A_J	937	697	MHz
B_{62}	−402	g_J	0.81	1.03	
B_{64}	−61	$\Lambda_{x_c x_c}$	0.0280	0.0066	cm
B_{66}	−52	$\Lambda_{y_c y_c}$	0.0140	−0.0090	cm
		$\Lambda_{z_c z_c}$	0.2000	0.0069	cm

$E_0 - E_1 = -82$ cm^{-1} and $E_2 - E_1 = 113$ cm^{-1}. The combination of matrix elements and energy differences results in smaller values for Λ_{ii} compared to the ground-state. This can also partly explain the isotropy of the excited state g_i values, which are closer to the nuclear Zeeman contribution. As pointed out above, several Pr^{3+}-doped compounds exhibit the same behavior so that the discussion given above could also be applied to them.

We now turn to the principal axes of the spin Hamiltonian tensors. The oscillator strengths are assumed to be proportional to the square of the overlap of the nuclear wave functions,[22] the latter being given by the ground- and excited state Hamiltonians, which is reasonable since the hyperfine interactions are a small perturbation to the electronic wave functions. Thus we can check the relative oscillator strengths following from our $(\alpha_Q, \beta_Q, \gamma_Q, D, E)$ parameters against values from zero-field spectral tayloring experiments.[19] The results are gathered in Table IV. A good agreement is found, showing that indeed the orientation of the quadrupole tensors was determined correctly. In Pr^{3+}:Y_2SiO_5, significant discrepancies were found between calculated and experimental values.[38,39] This was tentatively attributed to additional selection rules due to superhyperfine coupling with Y ions. In our case, it seems that although superhyperfine coupling may also be observed (see Sec. V D), relative optical transition matrix elements can still be determined from the overlap of the nuclear wave functions.

Hyperfine transition linewidths were also determined during the fit procedure. The data show (see Fig. 3) that the transitions with the larger splittings also show the larger linewidths. For example, the ground-state $|\pm\frac{3}{2}\rangle \leftrightarrow |\pm\frac{5}{2}\rangle$ transitions at 24.44 MHz have an average linewidth of 301 kHz, whereas the $|\pm\frac{1}{2}\rangle \leftrightarrow |\pm\frac{3}{2}\rangle$ transitions at 14.87 MHz have a width of only 105 kHz. This becomes reasonable if we focus on the dominant part of the Hamiltonian (Eq. (7)), $\mathcal{H}'' \approx D[I_{z_c}^2 - I(I+1)/3]$. In this case, the transition energies become $|\frac{1}{2}\rangle \leftrightarrow |\frac{3}{2}\rangle \approx |2D|$ and $|\frac{3}{2}\rangle \leftrightarrow |\frac{5}{2}\rangle \approx |4D|$. Crystal-field variations from one ion position to another correspond to a distribution of crystal-field parameters and therefore of the D parameter. The hyperfine linewidths should then be proportional to the transition energies. This is qualitatively in agreement with the experimental values. The excited state linewidths are also smaller than the ground-state ones, which suggests that the D distribution width is also proportional to D.

TABLE IV. Relative optical oscillator strengths between $^3H_4(0)$ and $^1D_2(0)$ hyperfine levels. Experimental[19] and calculated values, using Tables I and II, are being compared. Rows correspond to transitions starting from the ground-state hyperfine levels and columns correspond to transitions to different excited state hyperfine levels (see Fig. 1).

		$\lvert e,\pm\frac{1}{2}\rangle$	$\lvert e,\pm\frac{3}{2}\rangle$	$\lvert e,\pm\frac{5}{2}\rangle$
$\langle g,\pm\frac{1}{2}\rvert$	Exp.	0.09 ± 0.01	0.28 ± 0.01	0.63 ± 0.01
	Calc.	0.08 ± 0.01	0.24 ± 0.02	0.67 ± 0.02
$\langle g,\pm\frac{3}{2}\rvert$	Exp.	0.33 ± 0.01	0.39 ± 0.01	0.28 ± 0.02
	Calc.	0.31 ± 0.02	0.45 ± 0.02	0.24 ± 0.02
$\langle g,\pm\frac{5}{2}\rvert$	Exp.	0.55 ± 0.01	0.36 ± 0.01	0.09 ± 0.01
	Calc.	0.60 ± 0.02	0.31 ± 0.02	0.09 ± 0.01

D. Experimental verification of a ZEFOZ transition

As mentioned earlier, the coherence times for ZEFOZ transitions are expected to be much longer than at zero or arbitrary magnetic field. To our best knowledge this was demonstrated experimentally only for Pr^{3+}:Y_2SiO_5.[14,15] To verify our hyperfine characterization and also the usefulness of the ZEFOZ technique for other compounds, we present experimental data of a ZEFOZ transition of Pr^{3+}:$La_2(WO_4)_3$ in the following. Using our ground-state parametrization we sought for magnetic-field configurations and transitions that satisfy the ZEFOZ conditions[15]:

$$\vec{S}^I(\vec{B}_{\rm opt}) = \left(\frac{\partial \nu_i(\vec{B}_{\rm opt})}{\partial B_x}, \frac{\partial \nu_i(\vec{B}_{\rm opt})}{\partial B_y}, \frac{\partial \nu_i(\vec{B}_{\rm opt})}{\partial B_z} \right) = \vec{0}.$$

We identified the points $\vec{B}_{\rm opt}$ by numerical minimization of $|\vec{S}^I(\vec{B})|$ for all transitions ν_i within a magnetic-field grid. Several of the identified ZEFOZ transitions showed a low curvature, e.g., small second-order coefficients

$$S^{II}_{jk}(\vec{B}) = \left. \frac{\partial^2 \nu_i(\vec{B})}{\partial B_j \partial B_k} \right|_{\vec{B}}. \tag{10}$$

We studied the ZEFOZ transition at $\nu_4 = 12.6$ MHz and $\vec{B}_{\rm opt} = (57.5, 4.0, -36.1)$ mT. As the setup at TU Dortmund, described in Sec. III, was not designed for magnetic fields of more than 12 mT per axis, we carried out the ZEFOZ experiments at Lund University. This allowed for verification of the Hamiltonian parameters and predicted ZEFOZ points in an independent laboratory. The static magnetic-field vector was provided by a set of three orthogonal superconducting coils, suitable to generate the elevated field. Whereas the x and z coils could provide a resolution of ≈ 4 μT, the y-axis control was limited to a step size of 1 mT. To fit into the homogeneous region of the coils we cut the previously characterized crystal into a $5 \times 5 \times 1$ mm piece. This and the construction of the sample holder limited our alignment of the optical indicatrix to the coil frame to a precision of about 10° for the x and y axes. We could adjust the z axis much more precisely, aligning the reflection from the crystal surface normal to Z to be parallel with the incident laser. To find the ZEFOZ point experimentally we had to consider the alignment precision, the accuracy of the Hamiltonian parameters, and the calibration of the coils. In a first step we adjusted the magnetic field to get a good overlap between observed cw RHS spectra and the calculated line positions following from Table I and $\vec{B}_{\rm opt}$. Close to the ZEFOZ condition, the transition frequency becomes an insensitive tuning parameter for the field. Thus, in a second step we fine tuned the magnetic-field components by looking at the achieved spin coherence lifetime directly. For this we used a Raman-echo sequence[40] and tuned the field in order to maximize the echo signal for long evolution times (rf pulse separations). Figure 5 shows the longest-lived Raman-echo decay curves we could achieve. These demonstrate hyperfine coherence times of up to $T_2(\vec{B}_{\rm opt}) = 158 \pm 7$ ms, representing a 630-fold increase compared to the zero-magnetic-field situation.[20] The decay curves at magnetic fields slightly

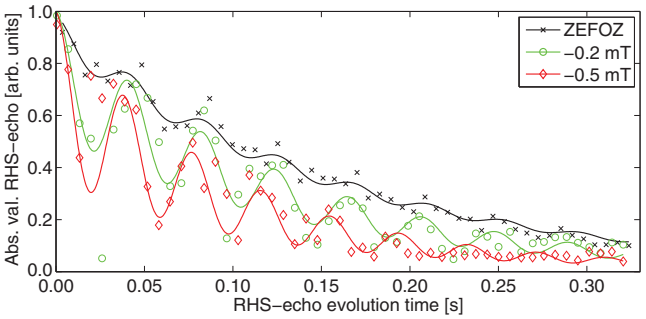

FIG. 5. (Color online) Raman-echo decays at the ZEFOZ point and with magnetic detunings of −0.2 and −0.5 mT for the z component.

detuned from the ZEFOZ point show slow modulations with a frequency of $\nu_M = 24.5 \pm 1.7$ Hz.[41] This could be due to a superhyperfine interaction with La nuclei, but a clear explanation is lacking at the present time. This point will be investigated in further experiments. As we moved the magnetic field away from the ZEFOZ point $\vec{B}_{\rm opt}$ by −0.2 mT in the z component, this resulted in a decrease of the coherence time to $T_2(-0.2\ {\rm mT}) = 133 \pm 16$ ms and a shift by −0.5 mT resulted in $T_2(-0.5\ {\rm mT}) = 97 \pm 19$ ms.

In the following we will use this measured $T_2(\vec{B})$ values to estimate the magnetic-field fluctuation at the Pr^{3+} site. These fluctuations cause frequency shifts and thereby broaden the hyperfine transition. For this purpose, we expand the hyperfine transition frequency ν_i on a deviation $B_{\rm off}$ from a given field $\vec{B}$:

$$\nu_i|_{\vec{B}} = \nu_i(\vec{B}) + s_1\, B_{\rm off} + \frac{s_2}{2}\, B_{\rm off}^2.$$

For $\vec{B} = \vec{B}_{\rm opt}$ the first derivative vanishes ($s_1 = 0$) and the frequency change due to small shifts is

$$\Delta\nu = \frac{s_2}{2} B_{\rm off}^2. \tag{11}$$

If the offset from the ZEFOZ condition is due to some random field ΔB, this leads to a line broadening instead of a frequency shift. The linewidth may then be written as

$$T_2^{-1} = \frac{s_2}{2}(\Delta B)^2. \tag{12}$$

With the experimentally obtained value of $T_2 = 158$ ms and $s_2 \approx 12$ kHz/mT^2, calculated from the maximum eigenvalue of the derivative matrix Eq. (10), using the parameters from Table I we thus estimate the magnetic-field fluctuations as $\Delta B \approx 32\ \mu$T.In Pr^{3+}:Y_2SiO_5 $\Delta B = 14\ \mu$T[14,16] ($s_2 \approx$ 3−6 kHz/mT^2) was found, representing the only ZEFOZ testbed experimentally investigated up to date. Thus both ΔB are of the same order and their values are compatible with the observed zero-field T_2 relaxation times [Pr^{3+}:$La_2(WO_4)_3 \approx$ 250 μs vs Pr^{3+}:$Y_2SiO_5 \approx$ 500 μs], noting that their g_i factors and thus their $s_1(B = 0)$ are comparable too.

When the deviation from $\vec{B}_{\rm opt}$ becomes large compared to the fluctuations, $B_{\rm off} \gg \Delta B$, Eq. (11) changes to

$$\Delta\nu = \frac{s_2}{2}\left(B_{\rm off}^2 + 2\Delta B\, B_{\rm off}\right). \tag{13}$$

The first term describes the line shift, the second a line broadening. For $\Delta B \approx 32\ \mu$T Eq. (13) yields a broadening corresponding to decay times $T_2(0.2\ {\rm mT}) \approx 13$ ms and $T_2(0.5\ {\rm mT}) \approx 5$ ms. Both T_2 values are significantly shorter than the experimental values. We account this to wrong assumptions for the model.

The most likely explanation for this discrepancy is that the relaxation at our reference field is not entirely due to magnetic-field fluctuations and that the reference field does not exactly fulfill the ZEFOZ condition. Both effects lead to additional contributions to the dephasing rate. We therefore write the total dephasing rate as

$$T_2^{-1} = T_{2,0}^{-1} + s_1\, \Delta B + s_2\, \Delta B\, B_{\rm off}. \tag{14}$$

Here $T_{2,0}^{-1}$ describes those contributions that are not due to magnetic-field fluctuations, such as phonons, while $s_1\, \Delta B$ accounts for a possible deviation of the experimental $\vec{B}_{\rm opt}$ from the exact ZEFOZ condition. Both terms are independent of $B_{\rm off}$ and are therefore indistinguishable in the available experimental data.

Using $s_2 \approx 8.2$ kHz/mT^2, which corresponds to the projection of Eq. (10) into the z direction, we now use Eq. (14) to estimate the magnetic-field fluctuations. The result of a linear fit of T_2^{-1} vs $B_{\rm off}$ yields $\Delta B \approx 1\ \mu$T. Applying the same analysis to the Pr^{3+}:Y_2SiO_5 data (estimated from Fig. 2 in Ref. 14) gives $\Delta B \approx 1.3\ \mu$T. This also reduces the estimate for ΔB by approximately 1 order of magnitude compared to the analysis where the minimum dephasing rate is assumed to originate entirely from the quadratic term of the magnetic-field fluctuations.[16]

For a complete analysis of all contributions to the relaxation, further measurements are necessary. Phononic contributions to T_2 could be determined from measurements at different temperatures, since s_1 and s_2 are independent of the latter. Measurements of T_2 at several deviations $\vec{B}_{\rm off}$ could help to estimate the numerical value of $s_1\, \Delta B$.

VI. CONCLUSION

We characterized the spin Hamiltonian of Pr^{3+}:$La_2(WO_4)_3$ for the electronic ground-state and one electronically excited state utilizing RHS spectra. Using a crystal-field analysis, we indicated the reasons for the measured tensor principal values and orientations. The relative oscillator strengths between the $^3H_4(0)$ and $^1D_2(0)$ hyperfine levels derived from our data agree well with those measured in earlier work.[19] Using our characterization we could predict the magnetic-field value at which a ZEFOZ transition occurs. We verified this condition experimentally in a second laboratory. By investigating the coherence properties of the ZEFOZ transition we estimated the order of magnetic fluctuations at the Pr^{3+} site (ΔB) and found evidence that it is smaller than expected. Besides observing characteristics similar to superhyperfine interaction, we could achieve an up to 630-fold increase of the coherence lifetime compared to zero field. The demonstrated $T_2 = 158 \pm 7$ ms and the relatively low second-order Zeeman coefficient show that even crystal systems with high-magnetic-moment density can have a high potential for quantum memory and information applications.

ACKNOWLEDGMENTS

The authors are grateful to J. J. Longdell and M. J. Sellars for useful discussions in preparation of the ZEFOZ measurements. This work was supported by the Swedish Research Council, the Knut & Alice Wallenberg Foundation, the Crafoord Foundation, and the EC FP7, Contract Nos. 228334 and 247743 (QuRep).

---

*marko.lovric@tu-dortmund.de

†philippe-goldner@chimie-paristech.fr

[1] J. J. Longdell, M. J. Sellars, and N. B. Manson, Phys. Rev. Lett. **93**, 130503 (2004).

[2] L. Rippe, B. Julsgaard, A. Walther, Y. Ying, and S. Kröll, Phys. Rev. A **77**, 022307 (2008).

[3] J. H. Wesenberg, K. Mølmer, L. Rippe, and S. Kröll, Phys. Rev. A **75**, 012304 (2007).

[4] M. Nilsson and S. Kröll, Opt. Commun. **247**, 393 (2005).

[5] M. Afzelius, C. Simon, H. deRiedmatten, and N. Gisin, Phys. Rev. A **79**, 52329 (2009).

[6] G. Hétet, J. J. Longdell, A. L. Alexander, P. K. Lam, and M. J. Sellars, Phys. Rev. Lett. **100**, 023601 (2008).

[7] R. Lauro, T. Chanelière, and J.-L. LeGouët, Phys. Rev. A **79**, 53801 (2009).

[8] M. P. Hedges, J. J. Longdell, Y. Li, and M. J. Sellars, Nature **465**, 1052 (2010).

[9] I. Usmani, M. Afzelius, H. de Riedmatten, and N. Gisin, Nature Comm. **1**, 1 (2010).

[10] M. Bonarota, J.-L. Le Gouët, and T. Chanelière, New J. Phys. **13**, 013013 (2011).

[11] C. Clausen, I. Usmani, F. Bussieres, N. Sangouard, M. Afzelius, H. de Riedmatten, and N. Gisin, Nature **469**, 508 (2011).

[12] E. Saglamyurek, N. Sinclair, J. Jin, J. A. Slater, D. Oblak, F. Bussieres, M. George, R. Ricken, W. Sohler, and W. Tittel, Nature **469**, 512 (2011).

[13] T. Böttger, C. W. Thiel, R. L. Cone, and Y. Sun, Phys. Rev. B **79**, 115104 (2009).

[14] E. Fraval, M. J. Sellars, and J. J. Longdell, Phys. Rev. Lett. **95**, 030506 (2005).

[15] E. Fraval, M. J. Sellars, and J. J. Longdell, Phys. Rev. Lett. **92**, 077601 (2004).

[16] J. J. Longdell, A. L. Alexander, and M. J. Sellars, Phys. Rev. B **74**, 195101 (2006).

[17] W. Tittel, M. Afzelius, T. Chaneliére, R. L. Cone, S. Kröll, S. A. Moiseev, and M. Sellars, Laser Photonics Rev. **4**, 244 (2010).

[18] R. D. Shannon and C. T. Prewitt, Acta Crystallogr. Sect. B **25**, 925 (1969).

[19] O. Guillot-Noël, P. Goldner, F. Beaudoux, Y. LeDu, J. Lejay, A. Amari, A. Walther, L. Rippe, and S. Kröll, Phys. Rev. B **79**, 155119 (2009).

[20] P. Goldner, O. Guillot-Noël, F. Beaudoux, Y. LeDu, J. Lejay, T. Chanelière, J. L. LeGouët, L. Rippe, A. Amari, A. Walther, and S. Kröll, Phys. Rev. A **79**, 33809 (2009).

[21] J. J. Longdell, M. J. Sellars, and N. B. Manson, Phys. Rev. B **66**, 35101 (2002).

[22] R. M. Macfarlane and R. M. Shelby, in *Spectroscopy of Solids Containing Rare Earth Ions*, *Modern Problems in Condensed Matter Sciences*, edited by A. A. Kaplyanskii and R. M. Macfarlane (North Holland, Amsterdam, 1987), Vol. 21, pp. 51–184.

[23] M. A. Teplov, Sov. Phys. JETP **26**, 872 (1968).

[24] H. Goldstein, C. P. Poole, and J. L. Safko, *Classical Mechanics* (Addison Wesley, San Francisco, 2002) p. 638.

[25] See Supplemental Material at http://link.aps.org/supplemental/10.1103/10.1103/PhysRevB.84.104417 for more details on conventions and the fitting procedure.

[26] O. Guillot-Noël, P. Goldner, Y. LeDu, P. Loiseau, B. Julsgaard, L. Rippe, and S. Kröll, Phys. Rev. B **75**, 205110 (2007).

[27] J. Mlynek, N. C. Wong, R. G. DeVoe, E. S. Kintzer, and R. G. Brewer, Phys. Rev. Lett. **50**, 993 (1983).

[28] N. C. Wong, E. S. Kintzer, J. Mlynek, R. G. DeVoe, and R. G. Brewer, Phys. Rev. B **28**, 4993 (1983).

[29] M. Mitsunaga, E. S. Kintzer, and R. G. Brewer, Phys. Rev. Lett. **52**, 1484 (1984).

[30] M. Mitsunaga, E. S. Kintzer, and R. G. Brewer, Phys. Rev. B **31**, 6947 (1985).

[31] S. Kirkpatrick, C. D. Gelatt, and M. P. Vecchi, Science **220**, 671 (1983).

[32] C. Audet and J. E. Dennis, SIAM J. Optim. **13**, 889 (2003).

[33] J. J. Longdell, Ph.D. thesis, Australian National University, 2003.

[34] O. Guillot-Noël, Y. LeDu, F. Beaudoux, E. Antic-Fidancev, M. F. Reid, R. Marino, J. Lejay, A. Ferrier, and P. Goldner, J. Lumin. **130**, 1557 (2010).

[35] A. Abragam, *The Principles of Nuclear Magnetism* (Oxford University Press, Oxford, 1994), p. 599.

[36] These parameters differ from those of Ref. 34, which correspond to another assignment of crystal-field axes.

[37] L. Esterowitz, F. J. Bartoli, R. E. Allen, D. E. Wortman, C. A. Morrison, and R. P. Leavitt, Phys. Rev. B **19**, 6442 (1979).

[38] M. Nilsson, L. Rippe, S. Kröll, R. Klieber, and D. Suter, Phys. Rev. B **70**, 214116 (2004).

[39] M. Nilsson, L. Rippe, S. Kröll, R. Klieber, and D. Suter, Phys. Rev. B **71**, 149902(E) (2005).

[40] The rf power was $P \approx 3$ W, the pulse lengths were $\tau_p \approx 25$ and 50 μs, respectively, and the rf coil axis was aligned along the z axis.

[41] We fit the decay times with the function $f(t) = [A + M\cos(2\pi\nu_M t)]\exp(-t/T_2) + c$, where A is the exponentially decaying part, ν_M is the modulation frequency, T_2 the decay time, and c an offset.

Supplemental material for: "Hyperfine characterization and spin coherence lifetime extension in Pr^{3+}:$La_2(WO_4)_3$"

Marko Lovrić,* Philipp Glasenapp, and Dieter Suter
Technische Universität Dortmund, Fachbereich Physik, 44221 Dortmund, Germany

Biagio Tumino, Alban Ferrier, and Philippe Goldner†
Chimie ParisTech ENSCP,
Laboratoire de Chimie de la Matiére Condensée de Paris(LCMCP),
75005 Paris, France
UPMC Univ Paris 06, 75005 Paris, France
CNRS, UMR 7574, 75005 Paris, France

Mahmood Sabooni, Lars Rippe, and Stefan Kröll
Department of Physics, Lund University, P.O. Box 118, S-221 00 Lund, Sweden
(Dated: August 30, 2011)

This supplemental material gives additional details concerning the implementation of the fitting procedure and the used conventions. It should be read in conjunction with the main manuscript and is no to be understood in a general context.

Please note: References to figures, sections and equations are relative to the main manuscript.

I. THE FITTING PROCEDURE

A. Source data

While it is possible to calculate directly the spectra from the Hamiltonian, the resulting amplitudes and phases do not agree with the experimentally observed values, since they depend strongly on experimental details, such as cable lengths, tuning curves etc. By far the most precise parameters of the spectra are the positions of the resonance lines. We therefore extracted these and used only the resonance frequencies as input to the actual fitting procedure.

For the extraction of the line positions, we fitted the absolute-value representation of the measured spectra to a series of gaussian-shaped resonance lines. To discriminate between real lines and noise or artifacts, we considered additional parameters like peak height, line width and noise level. For most of the recorded data the procedure worked satisfyingly, even for partially overlapping resonance lines. The positions of lines that had very small amplitudes or could not be fitted well due to strong overlapping were identified visually or omitted.

B. Fitting of Hamiltonian parameters

To fit the Hamiltonian parameters, such that the resulting line positions agreed with the experimental data, we first utilized a simulating annealing algorithm[1]. When the preliminary results of this step appeared to converge towards a global minimum, we switched to a pattern search algorithm[2], which polls meshes of adjacent points to find a better minimum. This reduced the necessity for an excessively long search at low temperatures in the simulated annealing procedure and represents an additional check for the quality of the minimum.

The implemented algorithm minimizes the RMS deviation between the measured and the calculated line positions of all spectra,

$$f_k^{RMS} = \sqrt{\sum_{N=1}^{N_{tot}} \frac{\sum_{i=1}^{Q_N} \left(\nu_{iN}^{exp} - \nu_{iN}^{k}\right)^2}{Q_N}}. \qquad (14)$$

For each of the N_{tot} spectra Q_N line pairs, consisting of the measured frequencies ν_{iN}^{exp} and the corresponding calculated frequencies ν_{iN}^{k} were identified. The index i runs over all lines in a single spectrum. Accordingly all possible eigenvalue differences (ν_{iN}^{k}) for the given Hamiltonian, derived from Eq. (2) and (5) using the given set of parameters of the k^{th} iteration and the N^{th} magnetic field orientation (Eq. (6)), were calculated.

Not all possible lines are always resolved or visible in the spectra (see e.g. Fig. 3). Therefore, we matched theoretical to experimental lines by minimizing the absolute deviations for this spectrum; each experimental line was associated only with a single theoretical line. Lines that could not be assigned uniquely were not considered in that step of the fitting procedure. This mapping could change during the fitting procedure, but in the final steps of the search, the procedure resulted in an unambiguous assignment.

We initialized the simulated annealing algorithm with a random guess for the parameters. At each following iteration one of the Hamiltonian parameters was randomly chosen and varied in an interval determined by the current temperature. If the variation resulted in a new minimum value of the RMS error, the new point was always accepted. If the variation was higher than the previous

minimum, the algorithm calculated the Boltzman factor

$$p_k = \exp\left(\frac{-\left(f_k^{RMS} - f_{k-1}^{RMS}\right)}{k_{B_l} \cdot T_{k_l}}\right) \qquad (15)$$

and compared it to a random number $p_r \,\epsilon\, [0,1]$. The new point was accepted for $p_k > p_r$ and rejected otherwise. The temperatures T_{k_l} are defined in the individual l-th parameter units. Conversion factors k_{B_l} ensured correct units and parameter independent scaling of the denominator in Eq. (15). All temperatures were lowered continuously as the fitting improved. This was done for all T_{k_l} in the same way, so that for simplicity we may speak in terms of a global temperature and omit the l-index where it is not necessary. At high temperatures the algorithm sampled a large parameter range. Enabling it to resettle in states of slightly higher misfits enables the algorithm to trace a large search-space and to avoid getting stuck in a local minima at the same time. As the temperature was gradually lowered, the parameter values became more confined in the vicinity of the global minimum.

C. Restrictions and Model

We chose the initial temperature T_0 such that the corresponding changes of the line positions were ≈ 10 times the inhomogeneous line widths. Typically $k_{max} \approx 10^6$ iterations for the simulated annealing lead to reliable results. Within the first 80% of the iterations the temperature was gradually lowered as $T_k \approx T_0\,(1 - k/k_{max})^2$. Then T_k was left constant at a value corresponding to a frequency uncertainty of a fraction of the typical linewidths (a few kHz).

During the whole fit, the parameters were constrained. As values for D and E can be derived from hole-burning experiments[3,4] their boundaries were restricted to $\pm 10\%$ of the literature values. We constrained the to gyromagnetic ratios to $\pm 100\%$ of the expected values of -(10-100) MHz/T observed in similar systems.[5,6,7] The Euler angles were allowed to vary over the whole definition range. The probability for choosing a specific parameter for the variation was proportional to the (relative) size of its boundaries. The new value of this parameter was chosen by adding a random value out of the interval $\pm T_{k_l}$. If the new value did not lie within the boundaries, the process was repeated. The final direct search was set up with the same boundaries and typically terminated after $5 \cdot 10^4$ iterations. As indicated before, we did not constrain the relative orientation of the quadrupole **Q**- and Zeeman **M**-tensor. To avoid ambiguous results, we had to fit all measured spectra of a single electronic state simultaneously. Due to the two non-equivalent sites this results in a maximum of 16 lines per spectrum.

II. EULER ANGLES CONVENTIONS

For the tensor transformations we used the common "zyz"-convention[8] with right-handed coordinate systems. The transformation matrices R, e.g. in Eq. (3) and (4), are given by:

$$A = \begin{pmatrix} \cos\alpha & \sin\alpha & 0 \\ -\sin\alpha & \cos\alpha & 0 \\ 0 & 0 & 1 \end{pmatrix}, B = \begin{pmatrix} \cos\beta & 0 & -\sin\beta \\ 0 & 1 & 0 \\ \sin\beta & 0 & \cos\beta \end{pmatrix}, C = \begin{pmatrix} \cos\gamma & \sin\gamma & 0 \\ -\sin\gamma & \cos\gamma & 0 \\ 0 & 0 & 1 \end{pmatrix}$$

$$R(\alpha,\beta,\gamma) = C \cdot B \cdot A = \begin{pmatrix} -\sin\alpha\sin\gamma + \cos\alpha\cos\beta\cos\gamma & \cos\alpha\sin\gamma + \cos\beta\cos\gamma\sin\alpha & -\cos\gamma\sin\beta \\ -\cos\gamma\sin\alpha - \cos\alpha\cos\beta\sin\gamma & \cos\alpha\cos\gamma - \cos\beta\sin\alpha\sin\gamma & \sin\beta\sin\gamma \\ \cos\alpha\sin\beta & \sin\alpha\sin\beta & \cos\beta \end{pmatrix}, \qquad (16)$$

with $\alpha,\ \gamma\ \epsilon\ [-\pi,\pi]$ and $\beta\ \epsilon\ [0,\pi]$.

* marko.lovric@tu-dortmund.de
† philippe-goldner@chimie-paristech.fr

[1] S. Kirkpatrick, C. D. Gelatt, and M. P. Vecchi, Science, **220**, 671 (1983).
[2] C. Audet and J. E. Dennis, Siam J. Optimiz., **13**, 889 (2003).
[3] O. Guillot-Noël, P. Goldner, Y. LeDu, P. Loiseau, B. Julsgaard, L. Rippe, and S. Kröll, Phys. Rev. B, **75**, 205110 (2007).
[4] O. Guillot-Noël, P. Goldner, F. Beaudoux, Y. LeDu, J. Lejay, A. Amari, A. Walther, L. Rippe, and S. Kröll, Phys. Rev. B, **79**, 155119 (2009).
[5] R. M. Macfarlane and R. M. Shelby, in Spectroscopy of Solids Containing Rare Earth Ions, Modern Problems in Condensed Matter Sciences, Vol. 21, edited by A. A. Kaplyanskii and R. M. Macfarlane (North Holland, Amsterdam, 1987) pp. 51–184.

[6] J. J. Longdell, M. J. Sellars, and N. B. Manson, Phys. Rev. B, **66**, 35101 (2002).

[7] The negative sign of the gyromagnetic ratios preserves the consistence with the crystal field analysis in Sec. V C. It should be noted that this analysis assumes a higher crystal symmetry than the actual one of Pr^{3+}:$La_2(WO_4)_3$ and that RHS spectra are not sensitive to the sign of the gyromagnetic ratios, as explained in Sec. IV.

[8] H. Goldstein, C. P. Poole, and J. L. Safko, Classical mechanics (Addison Wesley, San Francisco, 2002) p. 638.